NANO LETTERS
Letter
Cite This: *Nano Lett.* 2019, 19, 3830−3837
pubs.acs.org/NanoLett

Ion Write Microthermotics: Programing Thermal Metamaterials at the Microscale

Hwan Sung Choe,[†,‡,¶] Radhika Prabhakar,[§,¶] Geoff Wehmeyer,[∥,¶] Frances I. Allen,[†] Woochul Lee,[‡,⊥] Lei Jin,[†,‡] Ying Li,[#] Peidong Yang,[‡,⊥] Cheng-Wei Qiu,[#] Chris Dames,[∥,‡] Mary Scott,[†,∇] Andrew Minor,[†,∇] Je-Hyeong Bahk,[*,§] and Junqiao Wu[*,†,‡]

[†]Department of Materials Science and Engineering, University of California, Berkeley, California 94720, United States
[‡]Materials Sciences Division, Lawrence Berkeley National Laboratory, Berkeley, California 94720, United States
[§]Department of Electrical Engineering and Computer Science, University of Cincinnati, Cincinnati, Ohio 45221, United States
[∥]Department of Mechanical Engineering, University of California, Berkeley, California 94720, United States
[⊥]Department of Chemistry, University of California, Berkeley, California 94720, United States
[#]Department of Electrical and Computer Engineering, National University of Singapore, Singapore, 117583
[∇]The Molecular Foundry, Lawrence Berkeley National Laboratory, Berkeley, California 94720, United States

Supporting Information

ABSTRACT: Considerable advances in manipulating heat flow in solids have been made through the innovation of artificial thermal structures such as thermal diodes, camouflages, and cloaks. Such thermal devices can be readily constructed only at the macroscale by mechanically assembling different materials with distinct values of thermal conductivity. Here, we extend these concepts to the microscale by demonstrating a monolithic material structure on which nearly arbitrary microscale thermal metamaterial patterns can be written and programmed. It is based on a single, suspended silicon membrane whose thermal conductivity is locally, continuously, and reversibly engineered over a wide range (between 2 and 65 W/m·K) and with fine spatial resolution (10−100 nm) by focused ion irradiation. Our thermal cloak demonstration shows how ion-write microthermotics can be used as a lithography-free platform to create thermal metamaterials that control heat flow at the microscale.

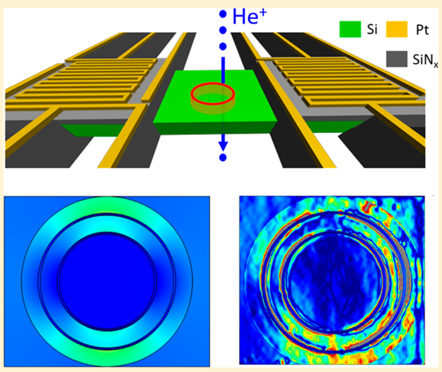

KEYWORDS: *Thermal metamaterial, thermotics, thermal conductivity, thermal cloak, ion irradiation*

Thermal metamaterials are heterogeneous structures designed to provide qualitatively new thermal functionalities that cannot be achieved in homogeneous, natural materials. At the macroscale, theoretical advances in transformation thermotics[1] have stimulated experimental demonstrations of various thermal devices to precisely route the heat flow in thermal cloaks,[2−4] shields,[5] camouflages,[6] inverters,[3] concentrators,[3] or thermostats.[7] These macroscopic devices utilize different materials with highly contrasting thermal conductivities (e.g., metals and polymers) that are mechanically integrated into the designed geometric pattern. One previous approach to scale these macroscopic thermal devices down to the microscale relies on drilling small holes in suspended crystalline membranes by nanopatterning with electron-beam lithography.[8] These holes contrast with the crystalline regions with zero thermal conductivity and enable the formation of binary composite thermal structures, similar to those of macroscopic devices; we refer to this configuration as "digital", because the thermal conductivity takes two discrete, fixed values in the composite. However, this approach is insufficient in general cases, and a different "analog" configuration is needed where more than two values, or even continuous variation of local thermal conductivity, are needed. For example, in order to implement a thermal cloak, there must be at least three distinct values of thermal conductivity available to block the heat from entering the cloaked object and to route the heat around the object.[2] However, mechanical integration of distinct materials at the microscale presents daunting technical challenges, and even if successful, mismatched thermal expansion and non-negligible thermal resistances at the interfaces between different materials would destroy the desired heat flow manipulation. Analog-like, continuously varied values of thermal conductivity could be mimicked by averaging over an area with different filling fractions of small holes, but this effective-medium approach is fundamentally incompatible with the microscopic length scales.

In this work, we develop a platform for ion-write microthermotics (IWMT), where a thin (∼120 nm),

Received: March 8, 2019
Revised: April 29, 2019
Published: May 6, 2019

DOI: 10.1021/acs.nanolett.9b00984
Nano Lett. 2019, 19, 3830−3837

suspended, single-crystal Si membrane is locally irradiated by a tightly focused (~1 nm) He^+ ion beam in a helium ion microscope (HIM) to create microscopic patterns. Depending on the dose of the irradiation, the local thermal conductivity (κ) of Si can be suppressed by more than 1 order of magnitude from the crystalline phase value to the amorphous phase value, as recently demonstrated in nanowires at room temperature.[9] The continuous tuneability of κ and the monolithic nature of the composite eliminate the aforementioned issues arising from the "digital" approach. The thermal conductivity suppression is also reversible upon a modest thermal annealing in a N_2 environment, offering reprogrammability of the IWMT. The IWMT provides a versatile platform with which microscopic patterns of thermal metamaterials can be designed and written to reroute local heat flow and achieve desired thermal functions. For example, we show that the IWMT enables thermal cloaking of objects that are 3 orders of magnitude smaller in size than in previous demonstrations.[3,4]

Figure 1a illustrates the device structure that demonstrates and characterizes the IWMT platform. The structure is based on the suspended micropad devices that were developed to measure the thermal conductivity of individual nanotubes,[10,11] nanowires,[12,13] and nanoribbons.[14] Here, a single-crystal Si membrane bridges two micropads suspended from the solid substrate by long and flexible SiN_x arms. The major difference from previous suspended micropad devices is that unlike in previous cases where the measured object is transferred to and bonded onto the two pads by focused ion beam (FIB) processing, here the Si membrane is monolithically integrated into the two pads via a Si base.[15] This design eliminates the thermal contact resistance[16] between the membrane (the heat channel) and the pads (the heat source and sink). As shown in Methods, convective and radiative heat losses from the pads and membrane are also negligible. Serpentine Pt electrodes were fabricated onto both pads and were electrically isolated from the Si base with a SiN_x layer. The Pt electrodes serve as both microheaters and thermometers for the thermal characterization of the Si membrane. The Si membrane (120 nm) is designed to be thinner than the projected stopping distance (242 nm with longitudinal straggle of 99 nm) of the 25 keV He^+ ions generated by the HIM (see SRIM simulation in Supporting Information), so that most of the irradiating ions pass through the Si membrane, leaving behind uniform lattice damage in the form of point defects of broken bonds and atomic interstitials and vacancies. The energy of the He^+ ions was chosen to be relatively low so as to maximize the nuclear stopping power (hence lattice damage) versus the electronic stopping power,[17] albeit not too low in order to avoid unwanted doping of the Si membrane with He atoms.

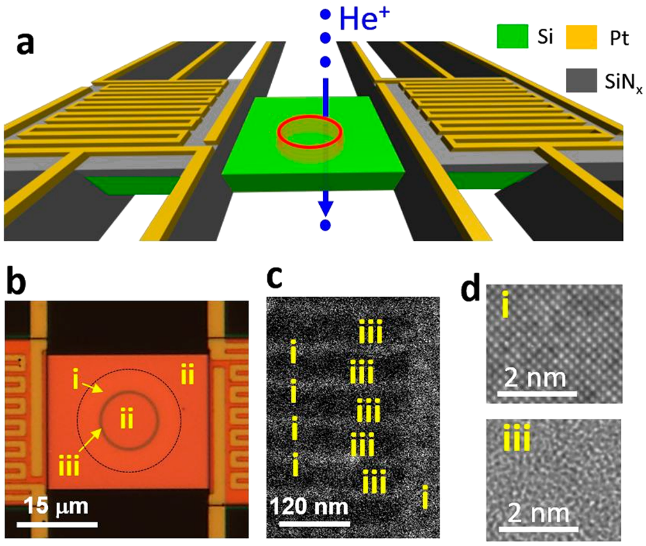

Figure 1. The IWMT platform created by local He^+ ion irradiation. (a) Schematic showing writing of local thermal conductivity in suspended single-crystal Si membrane using the He^+ ion beam. (b) Optical image of a real thermotic device consisting of a suspended Si membrane bridging two micropads. The Si membrane is patterned with a thin circle (region iii, darker reflection) at a heavy dose of 10^{18} ions/cm^2, a broader circle (region i) remaining pristine, and everywhere else (region ii) at a low dose of 5×10^{14} ions/cm^2. The outer boundary of region i is highlighted with a dashed circle to guide the eye. (c) SEM image of another Si membrane where a periodic pattern of pristine (region i)/heavily irradiated (region iii) is created with a period of 60 nm. (d) HRTEM images of a 30 nm thick Si layer irradiated with doses equivalent to regions i and iii in panel b, showing single crystal and amorphous Si phase, respectively.

After irradiation with the ion beam, the irradiated area appears darker in both optical (Figure 1b) and SEM (Figure 1c) images. Figure 1b shows an optical image of a suspended Si membrane, where circles were written with the ion beam. Figure 1c shows an SEM image of another pattern consisting of periodic pristine and heavily irradiated regions with a period of 60 nm. The tight focal spot size (~1 nm) of the ion beam and the small transverse straggle (see Supporting Information) allow a very fine spatial resolution (<100 nm in general, or <10 nm for doses <10^{15} ions/cm^2) of the features patterned onto the Si membrane. Transmission electron microscopy (TEM) analysis of the pristine (i) and heavily irradiated (iii) regions, as shown in Figure 1d, reveals that the heavily irradiated region becomes amorphous, which is in stark contrast to the single crystal phase in the pristine region. Such microstructural change of the membrane lays the material foundation for the device mechanisms of the IWMT platform, as analyzed in detail below.

Prior to device demonstration of the IWMT platform, we investigate the effects of He^+ ion irradiation on the thermal conductivity (κ) of the Si membrane. Figure 2a shows the experimentally measured variation of κ in response to the ion irradiation over a wide range of temperatures. Here the channel is uniformly irradiated by rastering the ion beam over the entire suspended part of the Si membrane between the

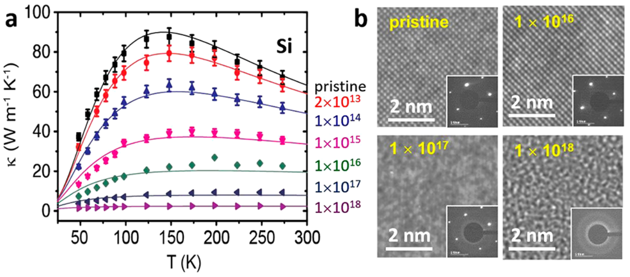

Figure 2. Modulating thermal conductivity using He^+ ion irradiation. (a) T-dependent thermal conductivity (κ) of the Si membrane after irradiation for a wide range of doses (in ions/cm^2). The curves are fits using a model including phonon scattering by defects, boundaries, and other phonons. (b) HRTEM images of a 30 nm thick Si layer irradiated with different doses. Insets: SAED pattern corresponding to the different doses of irradiation for 120 nm thick Si.

micropads; the irradiation dose is calculated from the beam current and irradiation time and area. The thermal conductivity measurements were performed inside a vacuum of <10^{-6} Torr to minimize the parasitic convection loss (see Methods for details). The Si membranes used for the κ measurements have typical widths of 2 μm, thicknesses of 120 nm, and lengths of 20 μm; these small widths were used to ensure accurate thermal resistance measurements for all sample irradiation levels (see Methods).

The pristine Si membrane shows a typical, nonmonotonic T-dependent κ with a room-temperature value of 65 ± 5 W/m·K, which is in good agreement with reported values in literature[18] for size-reduced single-crystal Si with comparable thickness. We note that as these membranes are only lightly doped with a resistivity above 20 Ωcm, the electronic contribution to κ is negligible and the measured κ is completely dominated by the phonon contribution. As the irradiation dose increases from 2×10^{13} to 1×10^{18} ions/cm^2, a monotonic suppression of $\kappa(T)$ is clearly observed. For example, at the dose of 10^{18} ions/cm^2, the room-temperature κ and peak κ are reduced from those of the pristine Si by a factor of 30 and 33, respectively. It is worth noting that in addition to the overall suppression of κ, the peak of $\kappa(T)$ shifts gradually toward higher temperatures, indicating increased scattering of phonons by defects and domains newly created in the crystal. The peak vanishes in the measurement temperature range (<300 K) for irradiation doses exceeding $\sim 10^{17}$ ions/cm^2, corresponding to amorphization of the Si membrane as shown later.

The suppression of κ in Figure 2a is quantitatively consistent with that in ref 9 where κ of irradiated Si nanowires was measured only at room temperature. In contrast, the κ suppression observed over the wide temperature range and peak shifts measured in this work provide much richer information regarding the suppression mechanism. In addition, the suppression of the pristine κ value is less severe for our membrane (room-temperature κ = 65 W/m·K for 120 nm film thickness) than for the previous Si nanowire geometry (room-temperature 50 W/m·K for 160 nm nanowire diameter),[9] which enables better heat transfer rates through the pristine region of the IWMT, an effect beneficial for heat flow control.

To further correlate the microstructural evolution of the material with the reduction in κ, we performed systematic high-resolution transmission electron microscopy (HRTEM) and selected area electron diffraction (SAED) analysis on the Si membranes after irradiation with different doses as shown in Figure 2b. For the pristine sample, the analysis confirms that the membrane is perfectly single crystalline with the (100) plane parallel to the membrane plane. The membrane remains single-crystalline after the irradiation with doses up to 10^{16} ions/cm^2. Beyond this dose, an amorphous phase starts to form inside the crystalline Si matrix, which becomes significant after 10^{17} ions/cm^2 irradiation. At $\sim 10^{18}$ ions/cm^2, the membrane is completely amorphized, as seen from the corresponding SAED pattern where the diffraction spots are lost and only diffusive rings are seen. This gradual evolution from point defects to amorphization of Si is consistent with previous demonstrations of ion-irradiation driven amorphization in Si.[19,20]

This analysis indicates that the suppression of κ is dominated by phonon scattering from point defects and amorphous domains in the low and high dose irradiation regimes, respectively. The measured $\kappa(T)$ was fitted by adopting a conventional model[21] that incorporates Umklapp, defects, and boundary scatterings using the Matthiessen's rule and the Born–von Karman dispersion for acoustic phonons. The impurity scattering is the only free parameter adjusted in the fitting, and the obtained impurity scattering rate increases monotonically with the irradiation dose, as shown in the Supporting Information. The data demonstrate the focused ion irradiation to be a powerful tool for engineering local thermal conductivity of materials from the single-crystal phase continuously to the amorphous level. The spatial resolution is ~100 nm for the suppression of κ by a factor of 30, or even below ~10 nm for κ suppression by a factor of 2 (see Supporting Information for spatial resolution discussion). Below we will also show that such engineering of κ is largely reversible.

The ability of the IWMT platform to route heat flux using these fine features enables the construction of a range of microscale thermal devices. A thermal shield routes heat fluxes around a small object via exquisite design of local thermal conductivity tensors, shielding the object from the external heat flux. A thermal cloak is a special type of shield that hides the object from far-field thermal detection, which requires rerouting the heat flow around the object while also mandating that the external heat flow is unchanged by the addition of the cloak and object.[2,3]

Thermal shield and cloak structures have been experimentally demonstrated at the macroscale (e.g., centimeters) using materials of contrasting thermal conductivity.[3,4] However, these macroscopic devices are too large to control heat flows at the microscale. Our IWMT approach provides a monolithic platform, on which the thermal shield and cloak can be readily constructed. Proving the function of these devices, however, requires spatial mapping of temperature over the entire device area, which is challenging at the microscale. We employ thermoreflectance imaging (TRI)[22−24] to map the temperature, which offers higher spatial resolution and temperature sensitivity than infrared thermography.

TRI is a noncontact optical technique for measurements of temperature variation on a surface by taking into account the change of optical reflectivity from the surface at different temperatures.[25,26] The relative change in reflectivity (ΔR) from the mean optical reflectivity (R) of a sample is related to the change in temperature (ΔT) of the surface using the thermoreflectance coefficient (C_{tr}) as $\Delta R/R = C_{tr}\Delta T$.[27−30] Because C_{tr} depends on the material, its surface roughness, and the wavelength of light used for measurement, it needs to be well calibrated for each sample prior to actual measurements.[27,28] The illumination wavelength chosen to maximizeC_{tr} is typically in the range of 400−800 nm, and is suitable for submicron imaging. All TRI in this work is performed using blue light (~470 nm), which is recommended for Si.[30] The thermal cloaks are microscopic suspended membranes which make it impossible to directly calibrate them using steady-state temperature cycling, typically used in determining C_{tr} of substrate-supported devices. For calibration of the suspended thermal cloaks, we use a transient calibration method, TransientCAL, which has been previously used in C_{tr} estimation of nanoscale features.[31] First, temperature cycling is used to determine a reference C_{tr} of a substrate supported material that is also present in the suspended heater pads. The thermal cloak is uniformly heated and cooled and transient thermal images of the suspended assembly (thermal cloak and the heater pads) are taken. Using the transient calibration method, these images and the reference C_{tr} is used for

DOI: 10.1021/acs.nanolett.9b00984
Nano Lett. 2019, 19, 3830−3837

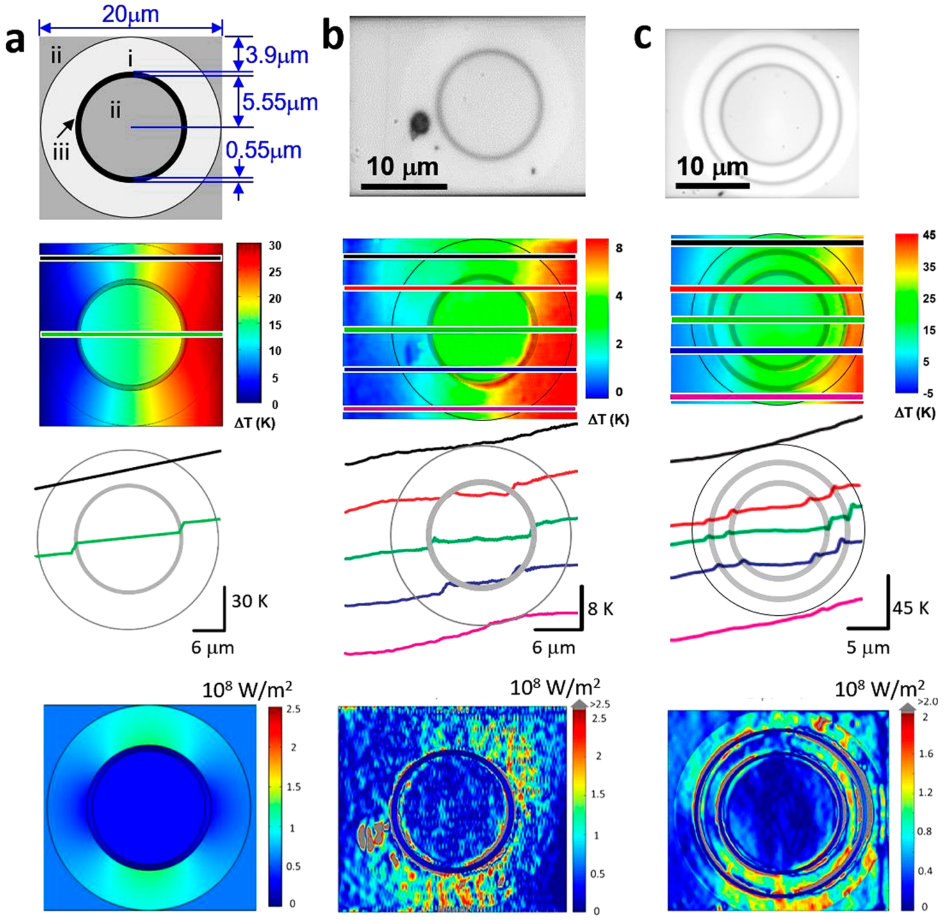

Figure 3. Thermal cloaks demonstrated with the IWMT platform. (a) Top to bottom: design of a bilayer thermal cloak. The concentric i, ii, and iii regions were irradiated with 0 (pristine), 5×10^{14}, and 1×10^{18} ions/cm^2, and have κ of 65, 40, and 2 W/m·K at room temperature, respectively; simulated temperature distribution $T(x,y)$ of the design where the right and left edges are set at 330 and 300 K, respectively; FEM-simulated temperature profile of the device along the straight lines indicated in the panel above; local heat flux map $|q_x(x,y)|$, obtained from Fourier's law $q_x = -\kappa\, \mathrm{d}T/\mathrm{d}x$. (b) Top to bottom: optical image of the bilayer thermal cloak realized on the IWMT platform following the design in a (the black dot is a dust particle contamination); temperature distribution of the device mapped by the TRI technique; measured temperature profile of the device along the straight lines indicated in the panel above; local heat flux map $|q_x(x,y)|$ obtained from Fourier's law. (c) Top to bottom: optical image of a quadlayer thermal cloak realized on the IWMT platform following the design in the Supporting Information; temperature distribution of the device mapped by the TRI technique; measured temperature profile of the device along the straight lines indicated in the panel above; local heat flux map $|q_x(x,y)|$ obtained from Fourier's law. The three regions of darkest, intermediate, and lightest contrast in the optical image were irradiated at 0, 2×10^{15}, and 1×10^{18} ions/cm^2 and have κ of 65, 30, and 2 W/m·K, respectively. The results in panels b and c show that the IWMT platform enables heat flux routing around the central region, as required for thermal cloaking.

obtaining a C_{tr} map of the thermal cloak. This is then used to extract the temperature map of the suspended thermal cloak (see Methods for measurement conditions and setup and the Supporting Information for details).

We first design a thermal cloak with two concentric rings (hence called "bilayer" design). Three distinct regions with different κ are created in the system as shown in the top panel of Figure 3a; κ values of regions i, ii, and iii are designed to be 65, 40, and 2 W/m·K at room temperature, respectively. Finite-element simulations (Figure 3a, second through fourth panels) show that such a device effectively shields the thermal flux around the central circle when it is thermally biased with a nearly uniform temperature distribution in the shielded region (see Methods). The numerical heat flux map $|q_x(x,y)|$ (Figure 3a, fourth panel) obtained from the temperature map $T(x,y)$ using Fourier's law confirms that the heat flux in the shielded region is very small. The larger heat flux in the pristine region of the cloak shows that the heat is efficiently routed around the shielded region, compensating for the additional thermal resistance of the low-conductivity region iii. As discussed in the Methods, the simulations predict that the total heat flow is changed by less than 1% through the addition of the cloak, and that the heat flow is only very weakly dependent on the thermal conductivity of the cloaked object (i.e., the innermost zone ii in Figure 1a).

An experimental bilayer thermal cloak is written on the Si membrane with the ion beam (Figure 3b) following the design pattern, and regions i, ii, and iii are irradiated with a dose of 0 (pristine), 5×10^{14}, and 1×10^{18} ions/cm^2, respectively. The temperature distribution of the system under thermal bias, mapped by the TRI technique (second and third panels in Figure 3b), shows that indeed the temperature in the middle circular region appears as a plateau with nearly isothermal distribution. Because the pristine region (region i) of the cloak has a higher thermal conductivity than the cloaked object, this indicates that the heat is mostly routed around the central region. The heavily irradiated region (region (iii) prevents the heat from leaking into the central region, as is required for thermal cloaking. The last panel of Figure 3b shows the experimental heat flux map $|q_x| = \kappa\left|\frac{dT}{dx}\right|$ obtained from the experimental T profile in the second panel of Figure 3b (see the Supporting Information for more details). This heat flux map demonstrates the thermal cloaking effect predicted by the simulations in Figure 3a. Lastly, it can be noted that the TRI temperature profiles and heat fluxes in Figure 3 display asymmetries that are not observed in the idealized thermal cloak simulations. The causes of this behavior are not fully understood, but could arise due to slight asymmetries in the device introduced during fabrication or due to nonuniform thermal tilts created during operation (see Supporting Information).

The IWMT platform can also be used to implement thermal cloak designs which have finer structural features than the simplest bilayer cloak. For example, Figure 3c shows a second device with a "quadlayer" design, in which two circular heat barriers instead of just one (as used in the first device) are fabricated. This quadlayer device is designed with three distinct values of κ of 65, 30, and 2 W/m·K, which were realized on the IWMT platform by irradiation at 0, 2×10^{15}, and 10^{18} ions/cm^2, respectively. TRI mapping in Figure 3c shows an enhanced uniformity of the temperature distribution in the inner circle compared to the bilayer design.

The experimental $|q_x(x,y)|$ maps for both the bilayer and quadlayer cloaks show that the heat flux magnitude is significantly larger in the pristine region of the cloak than in the central cloaked object, indicating efficient thermal cloaking. The numerical predictions for the quadlayer temperature profile and heat flux are shown in Figure S6. For the bilayer (quadlayer) cloak, the mean experimental heat flux within the cloaked region $\langle q_x \rangle = 1.6 \times 10^7$ Wm^{-2} (0.9×10^7 Wm^{-2}). These values represent factor of ~4 (~5) reductions compared to the predicted values in the absence of a thermal cloak, about 6×10^7 Wm^{-2} (4.5×10^7 Wm^{-2}). In Figure S7, we also show that the temperature gradient in the cloaked region of the quadlayer cloak is insensitive to the total heat flux imposed at the edge of the cloak, as expected.

Both the bilayer and quadlayer devices utilize the finely structured local thermal conductivity of the IWMT to bend heat flow around the central object. These designs necessitate the continuous control of thermal conductivity and monolithic integration of different constituents as achieved in the IWMT. Obviously, the IWMT can be configured to construct other types of thermal devices as well. In the Supporting Information, a classical thermal rectifier based on temperature-dependent thermal conductivities[32,33] is also demonstrated in the IWMT at 200 K, where the thermal conductance differs by 2.4% when the heat flow direction is reversed under a temperature bias of 30 K.

Lastly, we show that the suppression of κ in the IWMT is also reversible and rewritable. As shown in Figure 4a, the room-temperature κ is suppressed, relative to the original κ_{pristine} = 65 to 55 W/m·K ($\approx 0.85\kappa_{\text{pristine}}$) by irradiation of 10^{14} ions/cm^2. A moderate anneal of the device in an N_2 gas at 300 °C restores the suppressed κ to 62 W/m·K ($\approx 0.95\kappa_{\text{pristine}}$). For irradiation at higher doses, the suppression is greater whereas the recovery of κ is less. For example, after irradiation using 10^{15} ions/cm^2 (Figure 4b), κ is suppressed to 33 W/m·K = $0.51\kappa_{\text{pristine}}$, and annealing restores it to κ = 60 W/m·K = $0.92\kappa_{\text{pristine}}$. Importantly, after the initial annealing, the system appears to be locked into two stable states, such that subsequent treatments of irradiation and annealing under the same condition always set and reset κ between the low (33 W/m·K) and high (60 W/m·K) values. Therefore, akin to nonvolatile resistive random-access memory, the initial irradiation serves as a forming process, and the subsequent annealing and irradiation can repeatedly erase and encode the thermal conductivity distribution in the membrane.

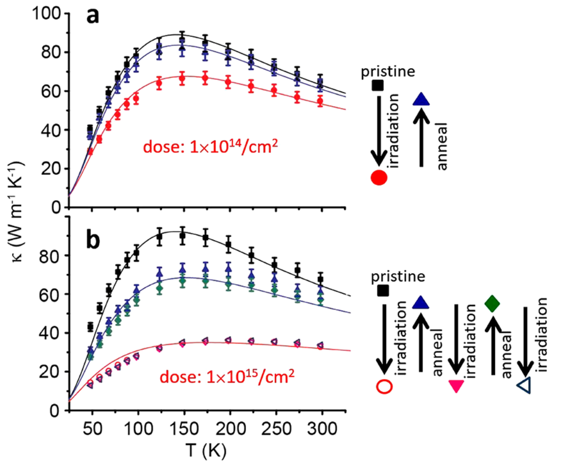

Figure 4. Reversibility and rewritability of the irradiation-engineered thermal conductivity. (a) $\kappa(T)$ curves of a pristine Si membrane, after He^+ ion irradiation (dose = 10^{14} ions/cm^2), and after anneal (300 °C in N_2 for 2 h). The anneal largely recovers the thermal conductivity. (b) The same for He^+ ion irradiation at a higher dose (10^{15} ions/cm^2) and sequential, repeated anneal-irradiation steps, showing the reversibility of the process after the first anneal. The curves are fitted lines using the model described in text and the Supporting Information.

In this work, a versatile platform is developed to reversibly write microscale thermal metamaterials. Using the platform, we experimentally demonstrate thermal cloaking at the microscale for the first time. The capability of controlling microscale heat flow using this platform opens opportunities to explore novel ideas for microscopic thermal management. As the spatial resolution of the ion writing is much smaller than that of the phonon mean free path (MFP) in crystalline Si (~50% of the heat carried by phonons with MFPs of at least 1 μm at room temperature, and longer for lower temperatures[34]), sub-MFP-sized devices can also be written onto the IWMT platform, which are potentially able to ballistically route thermal phonon transport for exploring exotic thermal effects beyond the Fourier law.[35,15] The gradual and controlled transition from the crystalline to amorphous phase in the IWMT also offers an ideal material system with which to test novel thermal conduction physics, such as the transition from thermal phonons to heat- carrying local vibration modes (or the so-called propagons and locons, respectively).[36] Using other ultrathin materials such as graphene[37] as the membrane, an even wider range of modulation of thermal conductivity could be achieved, which may enable improved performance or new functions. In this sense, the ion-write microthermotics demonstrated here has the potential to serve as a versatile platform with which to control heat flow at the microscale, akin to what nanofluidics does for fluids.

Methods. *Device Fabrication.* Fabrication of the suspended microdevices started with 6 inch silicon-on-insulator wafers (SOI) (vendor, SOITEC). The device layer of the SOI was lightly p-doped and single-crystalline with a resistivity of

20−30 Ω·cm, hole concentration of ~10^{15} cm^{-3}, (100) crystal orientation, and thickness of 200 ± 5 nm (thinned down to 120 nm in the final device). The buried silicon oxide layer and handle substrate were 200 ± 10 nm and 625 ± 10 μm thick, respectively. The silicon layer was patterned to define and form the silicon membrane below and between the two pads using photolithography (ASML 5500/300 DUV stepper) and a deep reactive ion etching process (SPTS ICP-SR deep reactive ion etcher). A 300 nm thick, Si-rich, low-stress SiN_x layer was deposited by low-pressure chemical vapor deposition, followed by metallization of 2 nm Cr and 50 nm Pt for the electrodes using sequentially the stepper photolithography, sputtering, and lift-off. Afterward, the SiN_x layer was patterned followed by reactive ion etching to expose the silicon membrane channel bridging the two pads. The wafer was cut into small chips of 9.2 × 9.2 mm in size, each containing 72 microdevices with silicon membrane channel of various lengths. After defining the width of the silicon membrane channel using electron beam lithography (Crestec CABL-9000) and ICP etching (Oxford PlasmaLab 150 inductively coupled plasma etcher) using hydrogen bromide, the devices were finally released from the substrate by backside photolithography and selective deep reactive ion etching.

Irradiation. The suspended Si membrane was irradiated by He^+ ions using a helium ion microscope (HIM, Zeiss ORION NanoFab). The incident ions were generated at the atomically sharp gas field-ionization source using a helium gas pressure of $\sim 2 \times 10^{-6}$ Torr. The acceleration potential and beam spot size were set to 25 kV and ~1 nm diameter (10 μm aperture), respectively. The irradiation doses were controlled by varying the beam current, dwell time, and scan spacing. A 2 pA beam current, 1 μs dwell time, and 0.25 nm scan spacing were used for most of the irradiation processes, except for the highest doses (10^{17} and 10^{18} ions/cm^2), which used a 10 nm spacing and 40 pA beam current (70 μm aperture). All patterns were designed and written using the NanoPatterning and Visualization Engine (NPVE) program from Fibics, Inc.

Thermal Conductivity Measurements. Thermal conductance (G) of the membrane was measured using the suspended micropad devices[11,13] placed in a cryostat with a vacuum chamber (pressure <10^{-6} Torr). Serpentine Pt electrodes predeposited on the two symmetric, suspended SiN_x pads act as microheater and thermometer for the thermal measurements. G was measured using the expression $G = (Q \times \Delta T_c)/[(\Delta T_h)^2 - (\Delta T_c)^2]$, where Q is the Joule heating power of the Pt microheater, and ΔT_h and ΔT_c are the temperature change of the hot and cold SiN_x pads, respectively.[11]

When a dc current (0−15 μA) flowed into the Pt microheater on the heating pad, ΔT_h and ΔT_c were simultaneously recorded by lock-in amplification of the Pt heater/thermometer resistance to an additional ac current (500 nA) applied to the microheater. The temperature coefficient of resistance (TCR) of the Pt heater/thermometer was precalibrated by quadratic fitting to its resistance as a function of global temperature prior to each measurement. The monolithic silicon device fabrication method ensures that there are no thermal contact resistances at the device−pad interface. The analysis of the measurement above assumes that the heating and sensing pads are isothermal; as discussed in the Supporting Information, this isothermal-pad analysis is valid in this scenario because the sample's thermal resistance (i.e., $1/G$) is always at least an order of magnitude larger than the spreading thermal resistance due to conduction near the pad−device interface. The thermal conductivity measured in this study has a <5% error, considering the errors of electrical measurements, as well as measurements of the sample dimensions.

TEM Characterization of Irradiated Silicon Membrane. HRTEM data was taken in an FEI Titan at 300 keV from a test Si membrane sample. The sample was irradiated to the same dose as the devices but was thinner (~30 nm, as opposed to 120 nm as in the devices) to allow for HRTEM imaging.

SAED data was taken in a Zeiss Libra TEM at 200 keV. Single devices with irradiated Si regions were mounted into an appropriate substrate using a low-temperature curing epoxy (200 °C). Using the pristine crystalline region of each film, the sample was tilted until the electron beam direction coincided with the Si ⟨100⟩ direction. Then, diffraction data was acquired for each radiation dose.

Thermoreflectance Imaging. The thermoreflectance coefficient (C_{tr}) was calibrated for the suspended materials following the established TransientCAL method presented in ref 31 followed by their steady-state thermal characterization. We used the TRI measurement setup (Microsanj NT-210B) in which an LED through a microscope objective illuminated the device under test (DUT) as it was biased, and a phase-locked CCD camera captured the reflectance signals from the surface of the DUT.[31,38] A blue-light LED (wavelength ~470 nm), which is suited to silicon devices, was used throughout the experiment with a 100×, 0.6 NA (numerical aperture) microscope objective. We determined the C_{tr} of a substrate supported platinum (Pt) contact pad using steady-state measurements by hot−cold temperature cycling. A 20 μs biasing pulse (at 2% duty cycle, total period 1 ms) was applied to both heaters and transient thermal images of the suspended assembly (Si membrane and heater pads) cooling to ambient temperature were captured up to 670 μs. These were used with the TransientCAL technique and a reference C_{tr} to obtain the calibration C_{tr} map of the membrane. We extracted the C_{tr} of a SiN_x region on the (suspended) heater using the Pt C_{tr}, and used this as the reference C_{tr} with the transient images to obtain the C_{tr} map by the TransientCal technique.[31] SiN_x, a rectangular area present on the (suspended) heater pad, was more suitable as the reference region than the narrow Pt serpentine region. After the calibration procedure, a 20 μs bias pulse was used to heat one side of the Si membrane to obtain thermoreflectance signals at the steady state operating temperature. These were used with the C_{tr} map to extract the heat flow across the device and obtain the final temperature map on the surface of the Si membrane.

The TRI measurements were done near room temperature. Convective heat loss from the device is estimated to be $\sim 10^{-6}$ W, which is much lower than the heat flux flowing in the Si membrane (about 10^{-4} W). Similarly, the temperature of the device was kept no more than ~350 K, and radiative heat loss is estimated to be less than 10^{-8} W.

Concept and Simulation of Thermal Cloak. Two-dimensional (2D) thermal cloaks hide thermal information about a cloaked object from far-field measurements in the 2D plane. To illustrate thermal cloaking, consider one-dimensional heat flow through a medium of thermal conductivity κ_m. If an object with a thermal conductivity $\kappa_o \neq \kappa_m$ is embedded in the medium, the steady-state temperature profile and heat flux vectors are modified. The goal of the thermal cloak is to restore the original 1D temperature profile and heat flows outside of the cloaked region, such that thermal measurements do not

DOI: 10.1021/acs.nanolett.9b00984
Nano Lett. 2019, 19, 3830−3837

reveal the presence of the cloaked object. Thermal cloaks achieve this restoration by routing the heat around the object without changing the magnitude of the total heat flow. Because the heat does not flow through the object, the cloaked object is ideally isothermal and the total heat flow is insensitive to κ_o.

Building on the designs of previously developed macroscopic thermal cloaks,[4] we designed microscale thermal cloaks with bilayer and quadlayer designs. We consider cylindrical thermal cloaks patterned into a background material that is lightly irradiated to achieve an intermediate conductivity κ_m (region ii in Figure 2). Thin layers of heavily irradiated Si with a low thermal conductivity κ_I (region iii) encircling the object provide insulation to prevent heat flow toward the cloaked object, whereas thicker cylindrical regions of pristine Si with a high thermal conductivity κ_P (region i) route the heat around the object. The rectangular background region has a length L along the direction of global heat flow x, width w in the orthogonal in-plane direction y, and thickness t. We perform 2D steady-state finite-element method (FEM) COMSOL simulations to find the temperature profiles and total heat flows through cloaked objects. We applied constant temperature boundary conditions at $x = 0$ and $x = L$ and adiabatic boundary conditions at $y = 0$ and $y = w$. We ensure mesh convergence by calculating the total heat flow in the x-direction and verifying that the total heat flow is converged to <0.01%.

From a design perspective, it is desirable to obtain large thermal conductivity contrast to enable efficient cloaking of large cloaked regions. For a given range of finite conductivity ratios and a certain cloaked object size, multiple cloak designs (e.g., bilayer, quadlayer, composite, or transformation-thermotic) can potentially be implemented; the design details and underlying theory of such cloaks have been previously discussed in the literature.[1,4,39] To compare the performance of the two cloak options selected for the IWMT demonstrations, we introduce several cloaking metrics. First, we want the total heat flow Q from the hot edge at T_h to the cold edge at T_c with the cloaked object present to be identical to the total heat flow through a homogeneous material with conductivity κ_m. Therefore, a perfect cloak would have $Q^* = \frac{QL}{\kappa_m tw(T_h - T_c)} = 1$. Second, we want Q to be insensitive to the value of the object thermal conductivity κ_o, demonstrating that the cloak is effective for many objects. One way to quantify this sensitivity is the dimensionless derivative $\delta = \frac{L}{wt(T_h - T_c)}\left(\frac{dQ}{d\kappa_o}\right)$ which should be small compared to unity. Lastly, we want the dimensionless temperature gradient at the center of the object $g = \frac{L}{(T_c - T_h)}\frac{dT}{dx}$ to be smaller than unity, indicating that the cloak is effectively rerouting the heat around the object. We note that using $\kappa_o = \kappa_m$ provides the most challenging cloaking test: if $\kappa_o \gg \kappa_m$, then g is always much less than 1 (even for a poor cloak) because the object is a "thermal short circuit" with no appreciable temperature gradients. Similarly, if $\kappa_o \ll \kappa_m$, then δ is always much less than 1 (even for a poor cloak) because the object is a "thermal open circuit" and all of the heat flows around the cloaked object.

For our final designs demonstrated in Figure 3, we selected the geometric parameters to optimize these cloaking metrics while ensuring that the object size was large enough to enable accurate TRI measurements and that the highly irradiated section was as small as possible. The limit on the highly irradiated thickness arises because the TRI signal displays artifacts due to irradiation-induced surface roughness. We found that our bilayer cloak design in Figure 3a with $\kappa_o = \kappa_m = 40$ W/m·K provides simulated cloaking values of $Q^* = 0.996$, $\delta = 0.07$, and $g = 0.50$. In particular, the small value of δ indicates that the measured Q is quite insensitive to the object's thermal conductivity, because in the absence of a thermal cloak this geometry has $\delta = 0.24$. The simulations of the quadlayer cloak shown in Figure 3c with $\kappa_o = \kappa_m = 30$ W/m·K displays similar cloaking capabilities ($Q^* = 1.07$, $\delta = 0.07$, and $g = 0.53$) as the bilayer cloak in Figure 2c. Lastly, we note that our simulations neglect the interfacial thermal boundary resistance R_i between the regions of different irradiation levels because R_i is expected to be many orders of magnitude smaller than the thermal resistances due to bulk conduction. For example, molecular dynamics simulations of the crystalline/amorphous silicon interface[40] found that $R_i = 0.2 \times 10^{-9}$ K m^2 W^{-1}, a thermal resistance which is smaller than the thermal resistance due to conduction through 1 nm of amorphous silicon. This insensitivity to R_i is another advantage of the IWMT platform compared to macroscopically assembled thermotic devices.

■ ASSOCIATED CONTENT

Ⓢ Supporting Information

The Supporting Information is available free of charge on the ACS Publications website at DOI: 10.1021/acs.nanolett.9b00984.

> Thermal conductivity modeling, SRIM simulation of ion irradiation, thermoreflectance (TRI) imaging operation, thermoreflectance coefficient (C_{tr}), calibration, and temperature mapping, TRI measurement uncertainty discussion, verifying validity of thermal conductivity measurement, demonstration of thermal rectification with IWMT, experimental heat flux mapping in the thermal cloaks, quadlayer thermal cloak simulations, negligible heat flux in the cloaked region at different levels of total heat flux (PDF)

■ AUTHOR INFORMATION

Corresponding Authors

*E-mail: wuj@berkeley.edu.
*E-mail: bahkjg@ucmail.uc.edu.

ORCID

Woochul Lee: 0000-0002-0911-961X
Peidong Yang: 0000-0003-4799-1684
Mary Scott: 0000-0002-9543-6725
Je-Hyeong Bahk: 0000-0002-5808-2227
Junqiao Wu: 0000-0002-1498-0148

Author Contributions

H.S.C., R.P., and G.W. contributed equally to this work. J.W. conceived this project and H.S.C. and W.L. fabricated the suspended microdevices. H.S.C. and F.I.A. performed the HIM irradiation. H.S.C. measured the thermal conductivity. M.S. and A.M. performed HRTEM and SAED analysis. R.P. and J.B. performed the TRI experiments. G.W. and C.D. performed the FEM simulation and thermal conductivity modeling. H.S.C., R.P., G.W., and J.W. analyzed the data and drafted the paper. All authors discussed the results and contributed to writing the manuscript.

Author Contributions

¶H.S.C, R.P., and G.W. contributed equally.

Notes

The authors declare no competing financial interest.

■ ACKNOWLEDGMENTS

This work is supported by NSF under Grant DMR-1608899. Work at the Molecular Foundry was supported by the Office of Science, Office of Basic Energy Sciences, of the U.S. Department of Energy under Contract No. DE-AC02-05CH11231. J.W. acknowledges support from the Tsinghua-Berkeley Shenzhen Institute (TBSI). G.W. acknowledges support from Grant DGE-1752814. Y.L. and C.-W.Q. acknowledge support from the Ministry of Education, Singapore (Project No. R-263-000-C05-112). C.W.Q. acknowledges financial support from the National Research Foundation, Prime Minister's Office, Singapore under its Competitive Research Program (CRP award NRFCRP15-2015-03). J.B. and R.P. thank Dustin Kendig for helpful discussions regarding TRI measurements.

■ REFERENCES

(1) Li, Y.; Shen, X.; Wu, Z.; Huang, J.; Chen, Y.; Ni, Y.; Huang, J. *Phys. Rev. Lett.* **2015**, *115*, 195503.

(2) Han, T.; Bai, X.; Thong, J. T. L.; Li, B.; Qiu, C.-W. *Adv. Mater.* **2014**, *26*, 1731−1734.

(3) Narayana, S.; Sato, Y. *Phys. Rev. Lett.* **2012**, *108*, 214303.

(4) Han, T.; Bai, X.; Gao, D.; Thong, J. T. L.; Li, B.; Qiu, C.-W. *Phys. Rev. Lett.* **2014**, *112*, 054302.

(5) Narayana, S.; Savo, S.; Sato, Y. *Appl. Phys. Lett.* **2013**, *102*, 201904.

(6) Li, Y.; Bai, X.; Yang, T.; Luo, H.; Qiu, C.-W. *Nat. Commun.* **2018**, *9*, 273.

(7) Shen, X.; Li, Y.; Jiang, C.; Huang, J. *Phys. Rev. Lett.* **2016**, *117*, 055501.

(8) Anufriev, R.; Ramiere, A.; Maire, J.; Nomura, M. *Nat. Commun.* **2017**, *8*, 15505.

(9) Zhao, Y.; Liu, D.; Chen, J.; Zhu, L.; Belianinov, A.; Ovchinnikova, O. S.; Unocic, R. R.; Burch Matthew, J.; Kim, S.; Hao, H.; Pickard, D. S.; Li, B.; Thong John, T. L. *Nat. Commun.* **2017**, *8*, 15919.

(10) Kim, P.; Shi, L.; Majumdar, A.; McEuen, P. L. *Phys. Rev. Lett.* **2001**, *87*, 215502.

(11) Shi, Li; Li, D.; Yu, C.; Jang, W.; Kim, D.; Yao, Z.; Kim, P.; Majumdar, A. *J. Heat Transfer* **2003**, *125*, 881.

(12) Hochbaum, A. I.; Chen, R.; Delgado, R. D.; Liang, W.; Garnett, E. C.; Mark, N.; Arun, M.; Yang, P. *Nature* **2008**, *451*, 163−167.

(13) Chen, R.; Hochbaum, A. I.; Murphy, P.; Moore, J.; Yang, P.; Majumdar, A. *Phys. Rev. Lett.* **2008**, *101*, 105501.

(14) Lee, S.; Yang, F.; Suh, J.; Yang, S.; Lee, Y.; Li, G.; Choe, H. S.; Suslu, A.; Chen, Y.; Ko, C.; Park, J.; Liu, K.; Li, J.; Hippalgaonkar, K.; Urban, J.; Tongay, S.; Wu, J. *Nat. Commun.* **2015**, *6*, 8573.

(15) Lee, J.; Lee, W.; Wehmeyer, G.; Dhuey, S.; Olynick, D. L.; Cabrini, S.; Dames, C.; Urban, J. J.; Yang, P. *Nat. Commun.* **2017**, *8*, 14054.

(16) Hippalgaonkar, K.; Huang, B.; Chen, R.; Sawyer, K.; Ercius, P.; Majumdar, A. *Nano Lett.* **2010**, *10*, 4341−4348.

(17) Nastasi, M.; Mayer, J. W.; Hirvonen, J. K. *Ion-Solid Interactions: Fundamentals and Applications*; Cambridge University Press:, New York, 1996.

(18) Marconnet, A. M.; Asheghi, M.; Goodson, K. E. *J. Heat Transfer* **2013**, *135*, 061601.

(19) Pelaz, L.; Marques, L. A.; Barbolla, J. *J. Appl. Phys.* **2004**, *96*, 5947.

(20) Ruault, M. O.; Chaumont, J.; Bernas, H. *Nucl. Instrum. Methods Phys. Res.* **1983**, *209-210*, 351.

(21) Yang, F.; Dames, C. *Phys. Rev. B: Condens. Matter Mater. Phys.* **2013**, *87*, 035437.

(22) Mayer, P. M.; Luerssen, D.; Ram, R. J.; Hudgings Janice, A. *J. Opt. Soc. Am. A* **2007**, *24*, 1156.

(23) Christofferson, J.; Shakouri, A. *Rev. Sci. Instrum.* **2005**, *76*, 024903.

(24) Maize, K.; Christofferson, J.; Shakouri, A. *Annual IEEE Semiconductor Thermal Measurement and Management Symposium*; IEEE: San Jose, CA, March, 2008 (DOI: 10.1109/STHERM.2008.4509366).

(25) Favaloro, T.; Suh, J.; Vermeersch, B.; Liu, K.; Gu, Y.; Chen, L.-Q.; Wang, K. X.; Wu, J.; Shakouri, A. *Nano Lett.* **2014**, *14*, 2394−2400.

(26) Ziabari, A.; Toores, P.; Vermeersch, B.; Xuan, Y.; Cartoixa, X.; Torello, A.; Bahk, J.; Koh, Y.i; Parsa, M.; Ye, P. D.; Alvarez, X.; Shakouri, A. *Nat. Commun.* **2018**, *9*, 255.

(27) Dilhaire, S.; Grauby, S.; Claeys, W. *Appl. Phys. Lett.* **2004**, *84*, 822.

(28) Farzaneh, M.; Maize, K.; Luerssen, D.; Summers, J. A.; Mayer, P. M.; Raad, P. E.; Pipe, K. P.; Shakouri, A.; Ram, R. J.; Hudgings, J. A. *J. Phys. D: Appl. Phys.* **2009**, *42*, 143001.

(29) Tessier, G.; Hole, S.; Fournier, D. *Appl. Phys. Lett.* **2001**, *78*, 2267.

(30) Yazawa, K.; Kendig, D.; Raad, P. E.; Komarov, P. L.; Shakouri, A. *Electronics Cooling Magazine* **2013**, *19*, 1.

(31) Kendig, D.; Hohensee, G.; Pek, E.; Kuang, W.; Yazawa, K.; Shakouri, A. *16th IEEE Intersociety Conference on Thermal and Thermomechanical Phenomena in Electronic Systems*; ITherm, 2017; Vol. 23.

(32) Hoff, H. *Phys. A* **1985**, *131*, 449−464.

(33) Dames, C. *J. Heat Transfer* **2009**, *131*, 061301.

(34) Esfarjani, K.; Chen, G.; Stokes, H. T. *Phys. Rev. B: Condens. Matter Mater. Phys.* **2011**, *84*, 085204.

(35) Ravichandran, J.; Yadav, A. K.; Cheaito, R.; Rossen, P. B.; Soukiassian, A.; Suresha, S. J.; Duda, J. C.; Foley, B. M.; Lee, C.-H.; Zhu, Y.; et al. *Nat. Mater.* **2014**, *13*, 168−172.

(36) Seyf, H. R.; Henry, A. *J. Appl. Phys.* **2016**, *120*, 025101.

(37) Ye, Z.-Q.; Cao, B.-Y. *Phys. Chem. Chem. Phys.* **2016**, *18*, 32952.

(38) Vermeersch, J.; Bahk, J.-H.; Christofferson, J.; Shakouri, A. *J. Appl. Phys.* **2013**, *113*, 104502.

(39) Narayana, S.; Sato, Y. *Phys. Rev. Lett.* **2012**, *108*, 214303.

(40) Lampin, W.; Nguyen, Q. H.; Francioso, P. A.; Cleri, F. *Appl. Phys. Lett.* **2012**, *100*, 131906.

Supporting information

Ion Write Micro-Thermotics: Programing Thermal Metamaterials at the Microscale

Hwan Sung Choe[1,2†], Radhika Prabhakar[3†], Geoff Wehmeyer[4†], Frances I. Allen[1], Woochul Lee[2,5], Lei Jin[1,2], Ying Li[6], Peidong Yang[2, 5], Cheng-Wei Qiu[6], Chris Dames[2, 4], Mary Scott[1, 7], Andrew Minor[1, 7], Je-Hyeong Bahk[3*], Junqiao Wu[1,2*]

[1] *Department of Materials Science and Engineering, University of California, Berkeley, California 94720, USA*

[2] *Materials Sciences Division, Lawrence Berkeley National Laboratory, Berkeley, California 94720, USA*

[3] *Department of Electrical Engineering and Computer Science, University of Cincinnati, Cincinnati, Ohio 45221, USA*

[4] *Department of Mechanical Engineering, University of California, Berkeley, California 94720, USA*

[5] *Department of Chemistry, University of California, Berkeley, California 94720, USA*

[6] *Department of Electrical and Computer Engineering, National University of Singapore, Singapore, 117583*

[7] *The Molecular Foundry, Lawrence Berkeley National Laboratory, Berkeley, California 94720, USA*

[†] These authors contributed equally to this work.

*Authors to whom correspondence should be addressed, Electronic addresses:

wuj@berkeley.edu and bahkjg@ucmail.uc.edu

Thermal conductivity modelling.

We model the thermal conductivity of silicon using the kinetic theory result $\boldsymbol{\kappa} = \frac{1}{3}\sum_p \int C_{\omega,p} v_{\omega,p} \Lambda_{\omega,p} d\omega$, where p indexes the phonon polarization, ω is the phonon frequency, $C_{\omega,p}$ is the volumetric modewise specific heat, $v_{\omega,p}$ is the group velocity, $\Lambda_{\omega,p} = v_{\omega,p}\tau_{\omega,p}$ is the mean free path, and $\tau_{\omega,p}$ is the scattering time. This expression for κ assumes that the phonon dispersion relation and scattering rates are isotropic, an assumption which is commonly employed when modeling thermally isotropic materials such as silicon.

We use the Born-von Karman isotropic approximation for the silicon phonon dispersion relation $\omega = \omega_0 \sin\left(\frac{2k}{\pi k_0}\right)$, where k is the phonon wavevector, $k_0 = (6\pi^2\eta_{PUC})^{1/3}$ is the Debye cutoff wavevector fixed by the experimental primitive unit cell density $\eta_{PUC} = 2.5 * 10^{23}\ \mathrm{m}^{-3}$ [1], and $\omega_0 = 2v_s k_0/\pi$ is fixed by the experimental speed of sound v_s. We obtain v_s by an unweighted averaged of the measured speeds of sound along the [100], [110], and [111] directions and obtain $v_{s,LA} = 8973\ \mathrm{m/s}$ for the longitudinal polarization and $v_{s,TA} = 5398\ \mathrm{m/s}$ for the two transverse polarizations [1].

We use Matthiessen's rule to combine the phonon-phonon (Umklapp) scattering rate τ_U^{-1}, boundary scattering rate τ_B^{-1}, and impurity scattering rate τ_I^{-1} as $\tau^{-1} = \tau_U^{-1} + \tau_B^{-1} + \tau_I^{-1}$. To model the phonon-phonon scattering, we use the relation $\tau_U^{-1} = P\omega^2 T \exp(-C_U/T)$ with the values $P = 1.9 * 10^{-19}\ \mathrm{s.K}$ and $C_U = 280\ \mathrm{K}$, which were obtained by a fit to temperature-dependent κ measurements of bulk silicon [2]. The film thickness and nanoribbon aspect ratio are used to calculate the boundary scattering mean free path for a rectangular nanowire assuming fully diffuse boundary scattering [3, 4]. The form of the impurity scattering rate is $\boldsymbol{\tau_I^{-1} = A\omega^4}$: for the bulk sample, $\boldsymbol{A = 2.5 * 10^{-45}\ s^3}$ .We obtain the impurity scattering strength $\boldsymbol{A}$ for each sample by fitting the measured $\boldsymbol{\kappa(T)}$. We note here that $\boldsymbol{A}$ is the only free fitting parameter in the model.

Suppplementary Table 1 shows the values of the impurity scattering strength parameter $\boldsymbol{A}$ as a function of the ion dose. Here, $\boldsymbol{A}$ was determined by fitting to the data shown in Fig 2 of the main text. $\boldsymbol{A}$ increases monotonically with ion dose, representing the enhanced scattering with increasing point defect concentration. Supplementary Table 2 shows the values of $\boldsymbol{A}$ used in the reversibility studies of Fig. 4a,b.

Dose (ions/cm^2)	Pristine	2×10^{13}	1×10^{14}	1×10^{15}	1×10^{16}	1×10^{17}	1×10^{18}
Impurity parameter $\boldsymbol{A}$ (10^{-45} s^3)	5.3	8.5	19	59	190	910	5500

Supplementary Table 1: Impurity scattering parameters as a function of ion dose used in thermal conductivity modeling in Fig. 2. A is the only free fitting parameter in the model.

Dose (ions/cm^2)	1×10^{14}	1×10^{15}
Pristine impurity parameter ***A*** (10^{-45} s^3)	5.5	4.8
Irradiated impurity parameter ***A*** (10^{-45} s^3)	14	67
Annealed impurity parameter ***A*** (10^{-45} s^3)	7	13.5

Supplementary Table 2: Impurity scattering parameters for pristine, irradiated, and annealed samples shown in Fig. 4.

SRIM simulation of ion irradiation.

Monte Carlo simulations were performed using the stopping and range of ions in matter (SRIM) and the transport of ions in matter (TRIM) programs [5] to evaluate and predict the lattice damage of the 25 keV He$^+$ ion irradiation into the 120-nm-thick Si membrane. Considering the spot size (~1 nm) of the focused He$^+$ ion beam, the irradiation dose was calculated by the accumulated number of incident ions. The simulation results listed in Table S3 and S4 and Figure S1 show that, (1) most of (> 99%) the incident He$^+$ ions penetrate through the entire thickness of the suspended Si membrane without chemically doping the material, and (2) the defects introduced by the ion irradiation distribute reasonably uniformly across the thickness of the membrane. These SRIM and TRIM simulations indicate that the 25keV He$^+$ ion writing has a lateral resolution that depends on both the film thickness and the irradiation dose, ranging from 10 nm (for low doses < ~ 10^{15} ions/cm^2) to ~100 nm (for high doses ~ 10^{18} ions/cm^2) for the 120-nm-thick Si membrane.

Irradiation dose (ions / cm^2)	Si vacancies / He ion	Backscattered He ions	Transmitted He ions
10^{16}	19.1	1.0%	99.0%
10^{17}	23.8	1.3%	98.7%
10^{18}	23.1	1.4%	98.6%

Supplementary Table 3: Simulated number of Si vacancies created per incident helium ion, and the percentage of backscattered and transmitted He$^+$ ions through the 120 nm-thick Si membrane. They add up to 100.0%, meaning that a negligible percentage of the He$^+$ ions stay embedded in the Si membrane.

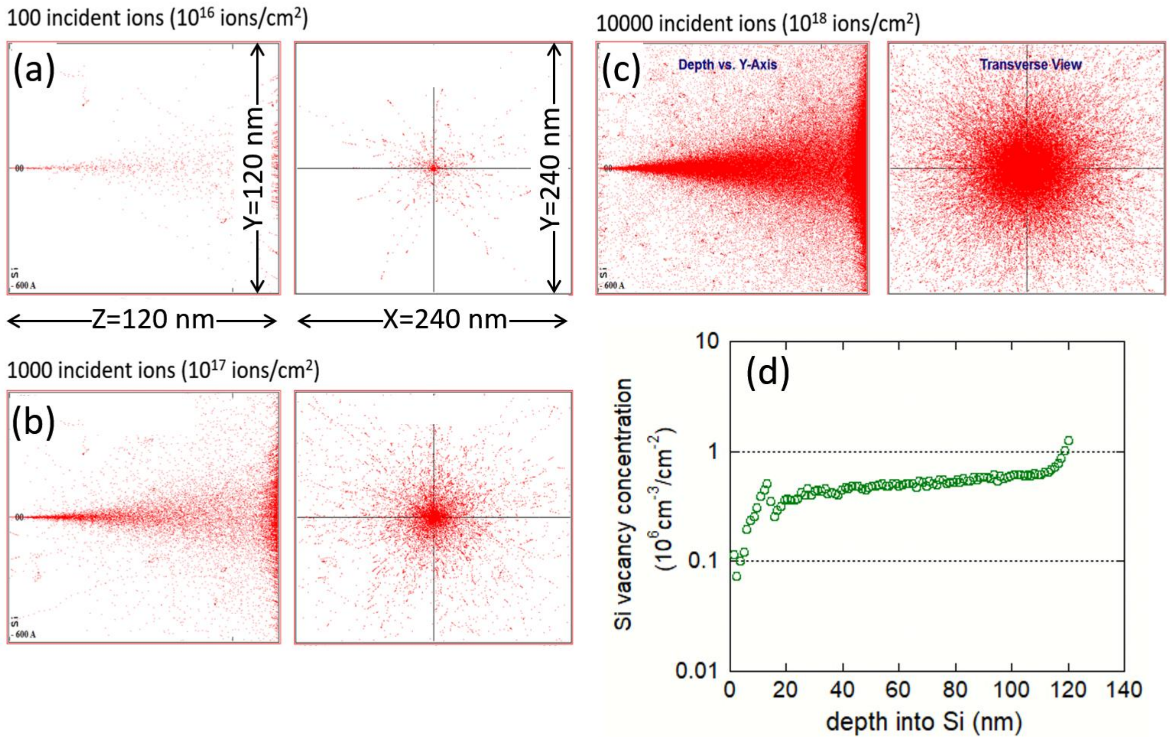

Figure S1: (a) – (c), SRIM simulated lattice damage when the 25keV He^+ ions are focused onto a single spot (< 1 nm) at a dose of 10^{16}, 10^{17} and 10^{18} ions/cm^2, respectively. The entire area shown is 120 nm × 120 nm for the longitudinal Y-Z plane (left panel) and 240 nm × 240 nm for the transverse X-Y plane at the back surface of the membrane (right panel). It can be seen that the lateral scattering of damage ranges from ~ 10nm to ~ 100nm depending on the dose, which defines the spatial resolution for the ion writing. (d) When the focused ion beam is rastered over the sample for laterally uniform irradiation, the simulated vacancies generated distribute reasonably uniformly over the membrane thickness. Here the vacancy concentration is given in cm^{-3}/cm^{-2}, meaning that the real vacancy concentration (in vacancies/cm^3) is this number multiplied by the irradiation dose (in ions/cm^2).

Thermoreflectance imaging (TRI) operation

The operation of the thermoreflectance imaging setup is briefly explained as follows.

The device under test (DUT) was biased for a certain time period and duty cycle. The LED light pulses were offset by a specific time delay relative to the device excitation. The CCD camera, exposure time of which was set up according to the device excitation, captured the reflected LED light from the device, thus storing reflected light variations from the hot and cold surfaces. Refer to Figure S2 for the timing diagram for this experiment. The system took a reference image at the LED delay of $t = 0$ with respect to the device excitation, which was used for image registration, alignment of the $t > 0$ images, and also for controlling the piezo stage for the xy and z drifts to prevent any long term drifting of the sample. Details of this setup and alignment procedures can be found in Reference [6].

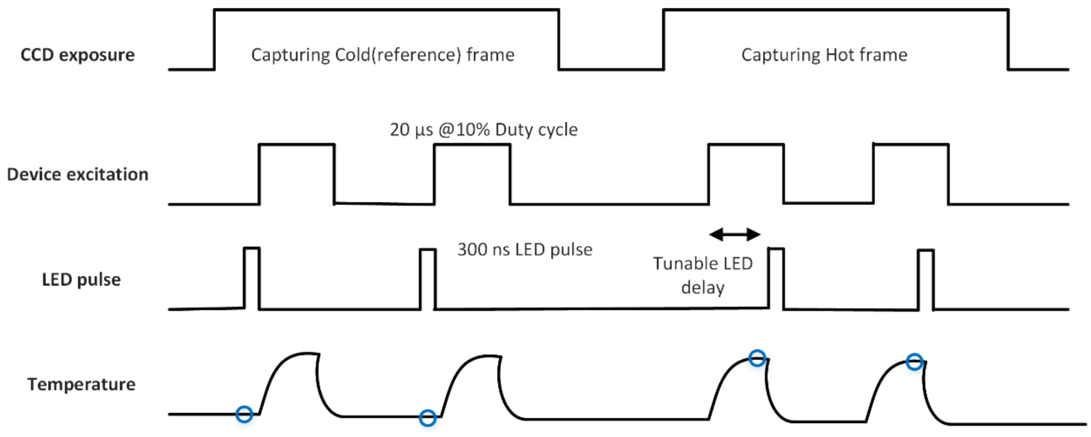

Figure S2: Timing diagram for capture of the reference (cold) image and the hot image. For our measurements, we used a 20 µs voltage pulse to bias the heaters and 300 ns LED pulse for illumination. Blue circles show that the cold (reference) image was taken just before the device was turned ON, and the hot image was taken when the device reached steady state temperature after being powered ON. The CCD exposure time was adjusted to capture both the hot and cold images.

Thermoreflectance coefficient (C_{tr}) calibration and temperature mapping.

C_{tr} calibration is done as a two-step process. First, steady state measurements are used for determining a single-value reference C_{tr} on a substrate supported material. Second, transient measurements, along with the reference C_{tr}, are used for obtaining a C_{tr} map on the suspended Si membrane. Thermal images are then taken at steady state temperatures and combined with the C_{tr} map to obtain the temperature distribution on the membrane.

Substrate supported devices with microscale features and larger allow simple global heating of device carrier / substrate while observing the temperature to obtain a C_{tr} map. Using a thermoelectric module or a heating stage, the device carrier is cycled between high and ambient temperatures to obtain the varying intensity ‘hot’ and ‘cold’ CCD frames.

For suspended MEMS devices, however, such a method for calibration is often not possible for the following reasons. First, isothermal heating of the device carrier does not allow for accurate temperature measurement on the membrane. The smallest thermocouples are 13-50 µm in size [7], using them for temperature measurement on the suspended heater pads or membrane is not possible due to the fragile nature of the device. Second, even if we somehow manage to measure the temperature *in situ*, there will be considerable edge effect artifacts caused by global thermal expansion. Global thermal expansion gains considerable importance at larger magnifications and when the feature sizes are in the sub-micron range. There is a considerable expansion of the heating stage and the thermal expansion of the sample interferes with the piezo stage corrections, thus leading to drifts and artifacts [6]. The smallest feature (ring linewidth) size in these devices is 500nm and 250nm for the bilayer and quadlayer metamaterial membrane, respectively. In such a case, local heating of the sample in question is most accurate.

We use the suspended heater pads for local heating of the Si membrane, with transient calibration technique [6], which involves capturing of a series of thermoreflectance images of device cooling after it reaches a peak temperature and is turned off. However, as will be seen in the description of this method below, the transient calibration method does need a reference C_{tr} for determining ΔT and extraction of C_{tr} map. We determine the C_{tr} of a Pt contact pad on the chip, which is substrate supported by steady state global heating. This is used to extract the (single-value) C_{tr} of the $\mathrm{SiN_x}$ on the suspended heater. We use this as the reference C_{tr} for extracting the thermal cloak map. $\mathrm{SiN_x}$, which is present as a larger rectangular area on the heater pad, is better suited for use with the *TransientCAL* method than the narrower serpentine Pt pattern (see Fig. S3a). The $\mathrm{SiN_x}$ C_{tr} value obtained by cycling the device on substrate between high and low temperatures was -5.0×10^{-4} K^{-1}.

Figure S3(a) shows the CCD image of the Si membrane and the heaters. For local heating, and to observe the thermal decay via transient thermoreflectance imaging, both heaters were equally biased to uniformly heat the membrane using a 20 µs (2% duty cycle) voltage pulse. The thermal cloak thus reached its peak temperature at 20 µs and began to cool subsequently. Using a larger duration pulse, for instance, 100 µs to ~1ms, led to large amount of heating of the suspended device, causing twisting and bending of the suspension, thus affecting the focus and reflectance data. We therefore used small duration pulse at 2% - 20% duty cycle to avoid overheating and allow for enough cooling time. We collected ~14 transient thermoreflectance images from ~20 µs to 670 µs separated by a time interval of 40 µs. Each image was averaged for 1000 seconds to minimize the noise.

Two $\mathrm{SiN_x}$ regions (blue and red regions on the heater in Figure S3(a)) were selected on the micro heaters to be used as reference microscale structures for the transient calibration. ΔT for these regions was ascertained by the reference C_{tr} value obtained above (-5.0×10^{-4} K^{-1}). The transient cooling temperatures for these regions can be seen in Fig. S4 (a). It can be seen that ΔT of these regions approached zero in a few hundred microseconds after the heaters are turned off. This is as expected and we used this value for transient calibration.

Assuming uniform heating of the suspended heaters and the Si membrane, this ΔT was used as a reference to determine the thermoreflectance coefficients on a pixel by pixel basis thus obtaining a C_{tr} map of the Si membrane using the *TransientCAL* method. Figure S3(b) shows the C_{tr} map of the membrane thus obtained.

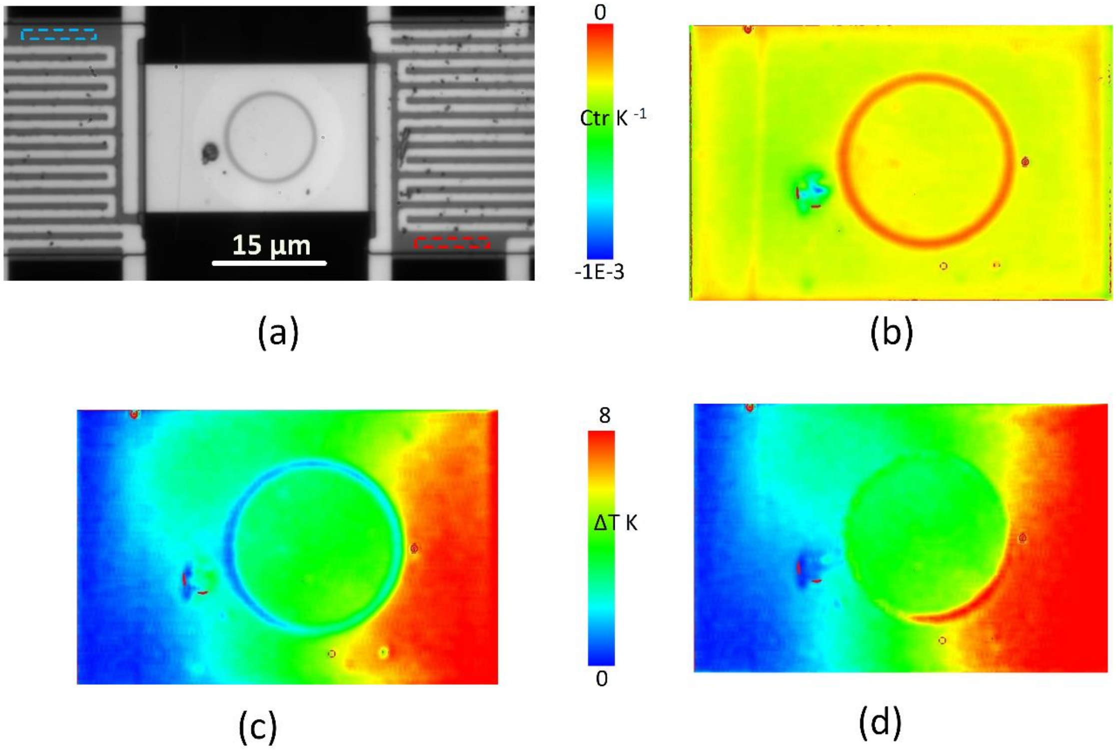

Figure S3: (a) CCD image of the suspended metamaterial Si membrane with the heaters. The dashed red and blue boxes show the SiN_x region, the ΔT of which was used as a reference for the transient calibration. (b) C_{tr} map obtained from the transient calibration method. (c) Raw thermoreflectance signal from the membrane when heating the right side (here the average Si C_{tr} is applied to obtain the ΔT), and (d) the actual temperature obtained on the surface of the membrane after application of the C_{tr} map. It can be seen that application of the C_{tr} map corrects for artifacts obtained on submicron features leading to more accurate temperature information, and one C_{tr} cannot be used for the complete membrane, reaffirming the need for a pixel-by-pixel C_{tr} calibration.

Next, thermal characterization of the metamaterial membrane at steady state temperature was done by turning on one of the heaters to observe the heat flow across the membrane. Thermal images were taken at 20 μs (at 10% duty cycle) when the devices reached their peak temperature (as shown by the simulation in Fig.S4(b)). A longer time averaging (~3600 seconds) was used for the capture of the data to reduce the noise. The raw thermoreflectance data is plotted in Figure S3(c), whereas (d) shows the actual temperature map after application of the C_{tr}.

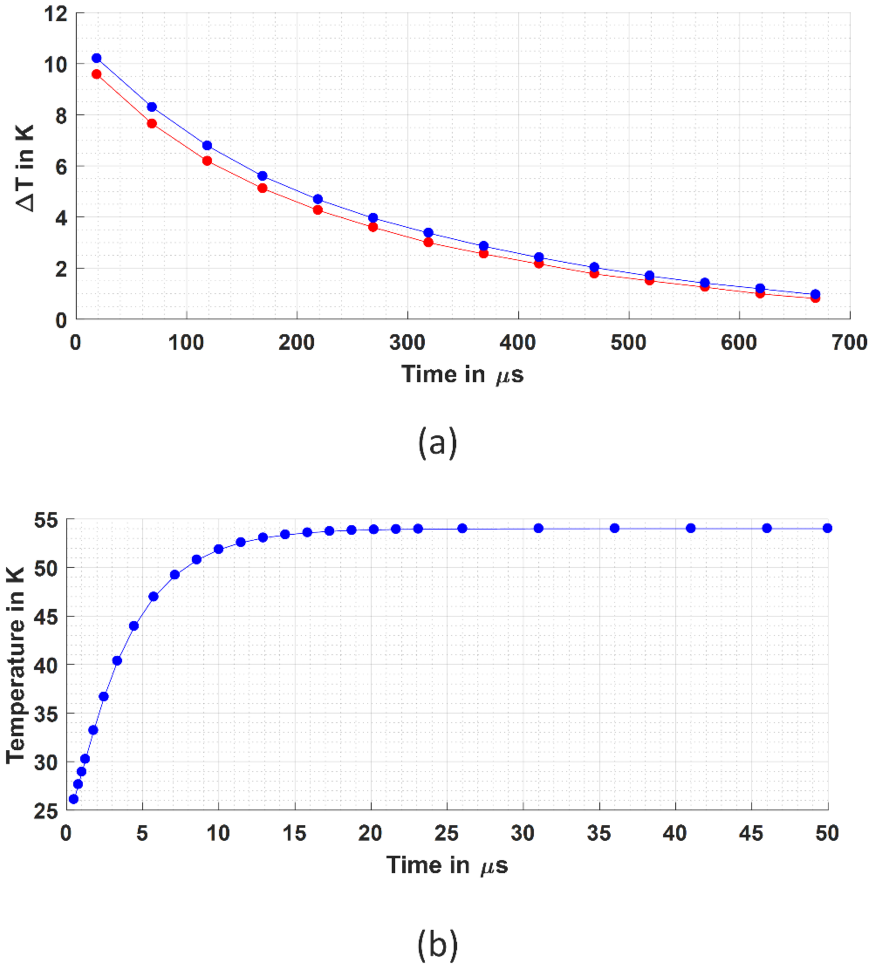

Figure S4: (a) Measured cooling of the left (blue) and right (red) SiN_x regions on the heater pad. They were heated for 20 μs and then turned off. The highest temperature can be seen at ~19 μs when the heater is ON, followed by subsequent cooling with the lowest ΔT ~ 669 µs. These temperatures were recorded using transient thermoreflectance imaging. (b) Simulation for the Si bilayer cloak shows that the device reaches a peak steady state temperature at ~20 µs. The FEM simulations were done in ANSYS for the device shown in Fig. 1b using the thermal conductivities of 2, 40, 70 W/m-K. This heating time was also used for measurements of the quadlayer cloak.

TRI measurement uncertainty discussion

To ensure high signal-to-noise ratios, TRI measurements are averaged over time, with typical averaging times being ~30 minutes or more. These long averaging times reduce the standard error of the measurement due to random noise to ~0.1K, as stated by TRI system specifications, and is similar to previous TRI measurements of bulk samples. Although this random error is appealingly small, averaging cannot eliminate potential uncertainties due to systematic errors or offsets (i.e. in general, measurements can be precise without necessarily being accurate). Surface roughness is one such systematic error source for TRI measurements [8]. Another potential source of error is device tilting. We now discuss the steps taken to minimize these potential systematic errors.

Surface roughness can affect the thermoreflectance coefficient because the incident light is not scattered specularly from the surface. To reduce the error due to surface roughness in the calibrations, the (single-value) calibration thermoreflectance coefficients C_{tr} of the SiN and the Pt pads are averaged over the largest possible pixel area available within the material analyzed. Care is taken to avoid edges and defects while selecting this averaging area. For the thermal cloak, a C_{tr} map is extracted using the transient calibration method and used with the reflectance map to obtain a pixel by pixel temperature map, fully accounting for non-uniformities in the thermoreflectance coefficient on the thermal cloak.

Another potential source of error is non-uniformity in the measurement of reflected light due to device tilts. To reduce this tilting effect, it is ensured that the TRI stage holding the device under test is levelled and isolated from vibrations. In addition, the TRI system used for these measurements includes piezo stages and auto focus to enable adjustments in case of device tilting and movement for small distances (~ 1 μm) and angles (~2 degrees). Furthermore, using local heating of the membrane for transient calibration reduces the impact of thermal expansion related effects, which are commonly seen for global heating calibrations and could potentially lead to drifts and artifacts.

Lastly, as discussed in the manuscript, the TRI images in Fig. 3 display noticeable asymmetries. Similar asymmetries were observed in TRI images of other thermal cloaks that we fabricated, and this temperature asymmetry was also seen in the same pristine device before patterning of the cloak (indicating that the cloak patterning process did not introduce the asymmetry). However, no asymmetries were observed in control TRI experiments for pristine devices which were supported on substrates (rather than being released and suspended), or on previous measurements for bulk samples. These control experiments indicate that the origin of the asymmetries could be due to the non-uniform thickness of the membrane (introduced before the cloak patterning), or due to non-uniform thermal tilts and built-in strains arising from the membrane release process. However, there might be other sources that contribute to the asymmetry as well, which warrants further investigation when studying temperature mapping of suspended membranes.

Verifying validity of thermal conductivity measurement

The underlying analytical model for extracting the device thermal conductance $\boldsymbol{G}$ from the measured data assumes that both the micro-heater and the sensor pads are isothermal. Of course, because heat is flowing from the pad to the sample, the pad can never be completely isothermal; however, if the device thermal resistance is sufficiently large, then the majority of the temperature drop occurs over the device, (rather than inside the pad), and the approximation is valid. In our experiments, the worst-case deviation from this idealized case would occur for the pristine device, which has a thermal resistance of $\boldsymbol{R}_{\mathbf{dev}} = \frac{\boldsymbol{L}}{\boldsymbol{\kappa w t}} = \mathbf{1.2 * 10^6}\,\frac{\mathbf{K}}{\mathbf{W}}$, where $\boldsymbol{L} = \mathbf{20\mu m}$ is the device length, $\boldsymbol{w} = \mathbf{2\ \mu m}$ is the device width, $\boldsymbol{t} = \mathbf{120\ nm}$ is the device thickness, and $\boldsymbol{\kappa} = \mathbf{67}\,\frac{\mathbf{W}}{\mathbf{mK}}$ is the pristine conductivity at room temperature. We estimate the thermal resistance due to heat flow constriction from the pad into the device to be $\boldsymbol{R}_{\mathbf{pad-device}} = \mathbf{9.2 * 10^4}\,\frac{\mathbf{K}}{\mathbf{W}}$; this estimate was obtained using an analytical solution for the constriction resistance between two rectangular channels with equal $\boldsymbol{\kappa}$ (Eq. 3.140 in Ref .[9]) for the case where the constriction ratio is equal to $\frac{\boldsymbol{w}}{\boldsymbol{w}_{\mathbf{pad}}}$, where $\boldsymbol{w}_{\mathbf{pad}} = \mathbf{30\ \mu m}$ is the pad width. This $\boldsymbol{R}_{\mathbf{pad-device}}$ estimate is conservative because it considers only heat transfer through the monolithic silicon portion of the pad, neglecting the parallel heat flow pathways through the SiNx and Pt on top of the pad, which would further reduce the thermal resistance of the pad. Therefore this analysis indicates that because the device thermal resistance $\boldsymbol{R}_{\mathbf{dev}}$ is at least an order of magnitude larger than the spreading resistance $\boldsymbol{R}_{\mathbf{pad-device}}$ in all cases, the isothermal pad approximation is reasonable. This conclusion is further supported by the good agreement between the measured pristine $\boldsymbol{\kappa}$ and previous silicon thin film measurements [10].

Demonstration of thermal rectification with IWMT

Thermal rectification, which occurs when heat flow experiences higher resistance in one direction than in the opposite direction, can be realized in a device called a thermal diode. Thermal diodes can find application, for example, in solid-state refrigeration cycle utilizing the magnetocaloric or electrocaloric effect. The thermal diode allows for strong thermal coupling when heat is pumped out of the refrigerator, while partially blocking undesirable heat backflow into the refrigerator during other portions of the cycle [11]. One way to realize the thermal rectification is a "junction thermal diode”, consisting of two segments with $\kappa(T)$ that have very different temperature trends [12, 13]. According to Ref.[13], in the ideal case when the thermal resistances of the left and the right segments are matched, and if their thermal conductivities depend on temperature as $\boldsymbol{\kappa_L(T) \propto T^{n_L}}$ and $\boldsymbol{\kappa_R(T) \propto T^{n_R}}$, it is expected that the thermal rectification is proportional to the temperature bias as $\boldsymbol{\gamma = \frac{(n_L - n_R)}{4}\Delta}$. Here $\boldsymbol{\gamma = \frac{Q_{LR} - Q_{RL}}{Q_{LR}}}$ is the thermal rectification, and $\boldsymbol{\Delta = \frac{T_H - T_C}{\frac{1}{2}(T_H + T_C)}}$ is dimensionless thermal bias. In these equations, the subscription “L” and “R” stand for the left- and the right-hand side, respectively, and “H” and “C” stand for the hot and cold side, respectively.

The Si membrane in the IWMT can be irradiated with different doses to form a junction thermal diode. As shown in Fig. S5(b), the membrane was irradiated in the two segments with 10^{14} and 10^{18} ions/cm^2 doses, which provided a ratio in κ of 28.5 at 200 K. For maximal thermal rectification, the length ratio of the two segments was set also at 28.5. A thermal rectification ratio of 2.4% was observed at 200K with 30K temperature bias of the device, as shown in Fig. S5(c). Fitting of the data in Figure S5(c) and (d) yields $\boldsymbol{\gamma = 0.16\,\Delta}$.

The $\kappa(T)$ data in Fig.S5(a) gives best-fit temperature dependence of $\boldsymbol{\kappa_L(T) \propto T^{-0.37}}$ and $\boldsymbol{\kappa_R(T) \propto T^{0.24}}$ near 200 K. Hence, a relationship of $\boldsymbol{\gamma = 0.15\,\Delta}$ is expected. This is in good agreement with the experimental data in Fig.S5(e).

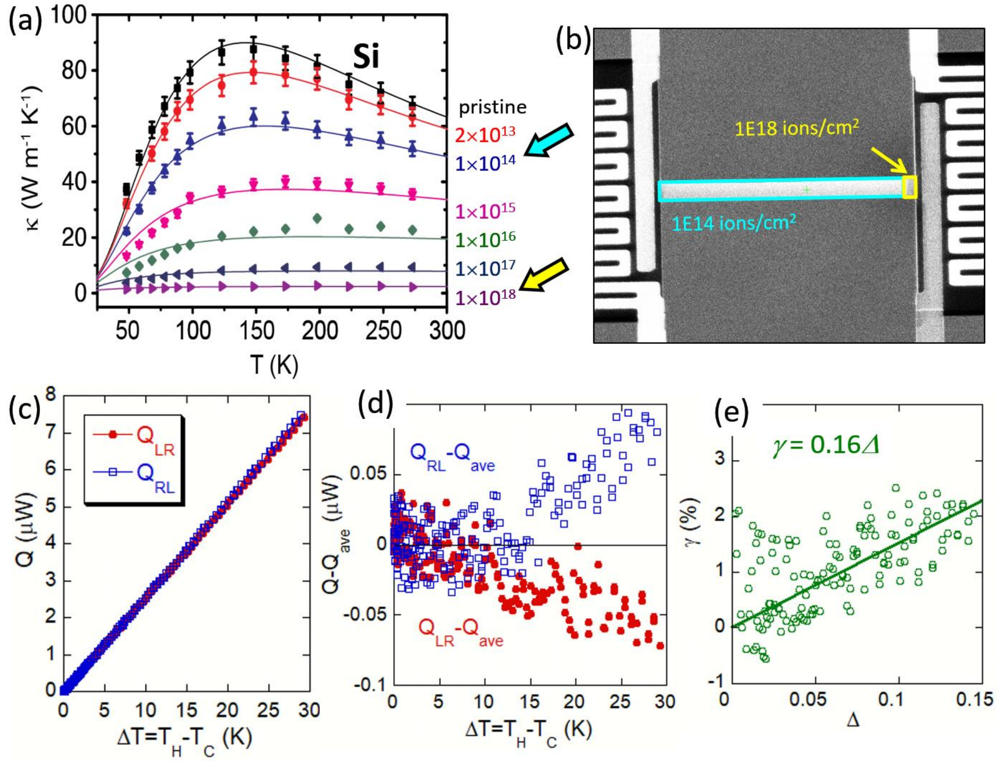

Figure S5: A thermal diode created by selective He$^+$ ion irradiation. (a) Thermal conductivity of the Si membrane as a function of temperature for various irradiation doses. Arrows show the two doses that are used for irradiation in the diode demonstration. (b) SEM image of the selectively irradidated Si membrane creating two segments of 10^{14} and 10^{18} ions/cm^2 doses, respectively. The membrane is 30 μm long and 2.3 μm wide. (c) Heat flow through the device (Q) as a function of temperature bias (ΔT) at a base temperature of 200 K. Blue (red) data points correspond to the case of heat flow direction from right (left) to left (right). (d) The heat flow asymmetry Q-Q_{ave} plotted as a function of ΔT, where $Q_{\mathrm{ave}} = (Q_{\mathrm{LR}}+Q_{\mathrm{RL}})/2$ is the averaged heat flow. (e) Experimentally measured thermal rectification (γ) as a function of dimensionless thermal bias (Δ). The line is a linear fit, which yields $\gamma = 0.16\mathit{\Delta}$, in good agreement with the theoretical prediction of $\gamma = 0.15\mathit{\Delta}$.

Experimental heat flux mapping in the thermal cloaks

Thermal cloaks route heat flow away from the cloaked object, meaning that the magnitude of the heat flux should be much larger in the cloak region than within the central cloaked object. We illustrate this heat flux routing using our experimental TRI temperature map $T(x, y)$ to obtain a local heat flux map $q_x(x, y)$. First, we smooth the TRI $T(x, y)$ image before evaluating $\frac{dT}{dx}$ numerically using a central-difference method. Smoothing the data by taking a moving average of the temperature profile over a square 600 by 600 nm averaging window reduces the variation in $\frac{dT}{dx}$ due to experimental noise. To obtain $\kappa(x, y)$ for regions (i), (ii) and (iii), we use our experimentally measured values of κ for uniformly irradiated silicon membranes of the same film thickness and dose. We then obtain the x-direction heat flux $q_x(x, y)$ using Fourier's law, $q_x = -\kappa \frac{dT}{dx}$.

In Fig. 3 of the main text, we plot the magnitude $|q_x(x, y)|$ over a limited range of values to emphasize the difference between the heat flux in the central object and in the pristine regions of the cloak. The clipped values of $|q_x(x, y)|$ which are larger than the upper range of the color map are represented in gray rather than in color. Most of these clipped regions have large values of $|q_x(x, y)|$ due to experimental artifacts from contamination or from the TRI temperature measurements within the heavily irradiated region (iii). We chose to plot the magnitude of the x-component of the heat flux q_x in Fig. 3, rather than the magnitude of the total heat flux $q = \|\kappa \nabla T\|$ because we found that q_x was less sensitive than q to edge effects in the numerical derivative near the edges of the suspended membrane.

Quadlayer thermal cloak simulations

In addition to the bilayer cloak shown in Fig. 2a and Fig. 2b, we also designed a quadlayer cloak with two separate irradiated regions. The experimental results for the temperature and heat flux are shown in Fig. 3c, and the numerical predictions are shown in Fig. S6. For this device, $L =$ 30 µm, $w =$ 25 µm, and the radius of the inner region is 6.9 µm. The radial width of each irradiated region is 350 nm, and the thickness of each pristine region is 2.45 µm.

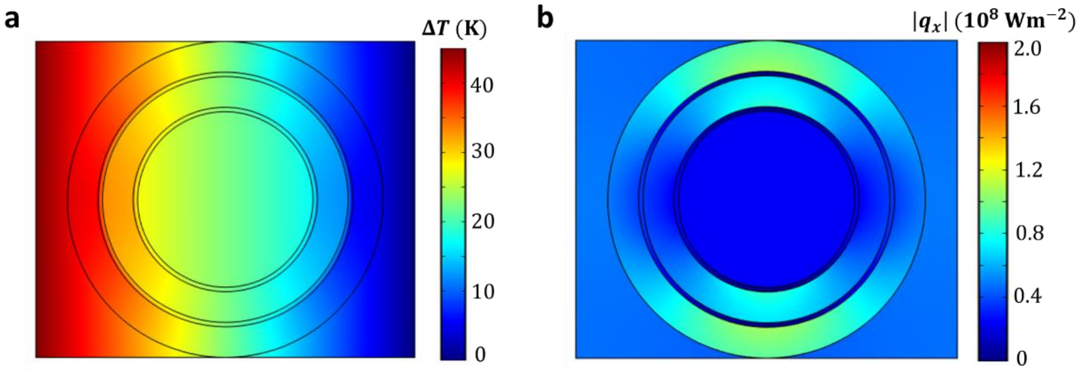

Figure S6: Simulated (a) temperature profile and (b) heat flux $\boldsymbol{q_x}$ maps for the quadlayer cloak.

Negligible heat flux in the cloaked region at different levels of total heat flux

We applied different heat fluxes to the quadlayer thermal cloak, and observed the temperature maps using TRI. Figure S7 shows that with increase in temperature bias, the heat flux through the membrane increases, but the temperature gradient in the cloaked region remains nearly the same, proving the thermal cloaking capability of the device.

The temperature vs. position linecut in Fig S7 shows dips in temperature profile in and around the high irradiation intensity rings due to artifacts. With the dimensions of the the rings being close to diffraction limits (TRI measurements use blue light of λ= 470 nm and the thickness of the rings for the quadlayer device is ~250 nm), edge effects from these features and their boundaries lead to incorrect temperature estimation at these regions. In the absence of these artifacts, the black dashed lines would indicate a close estimation to the temperature gradient on the highly irradiated regions.

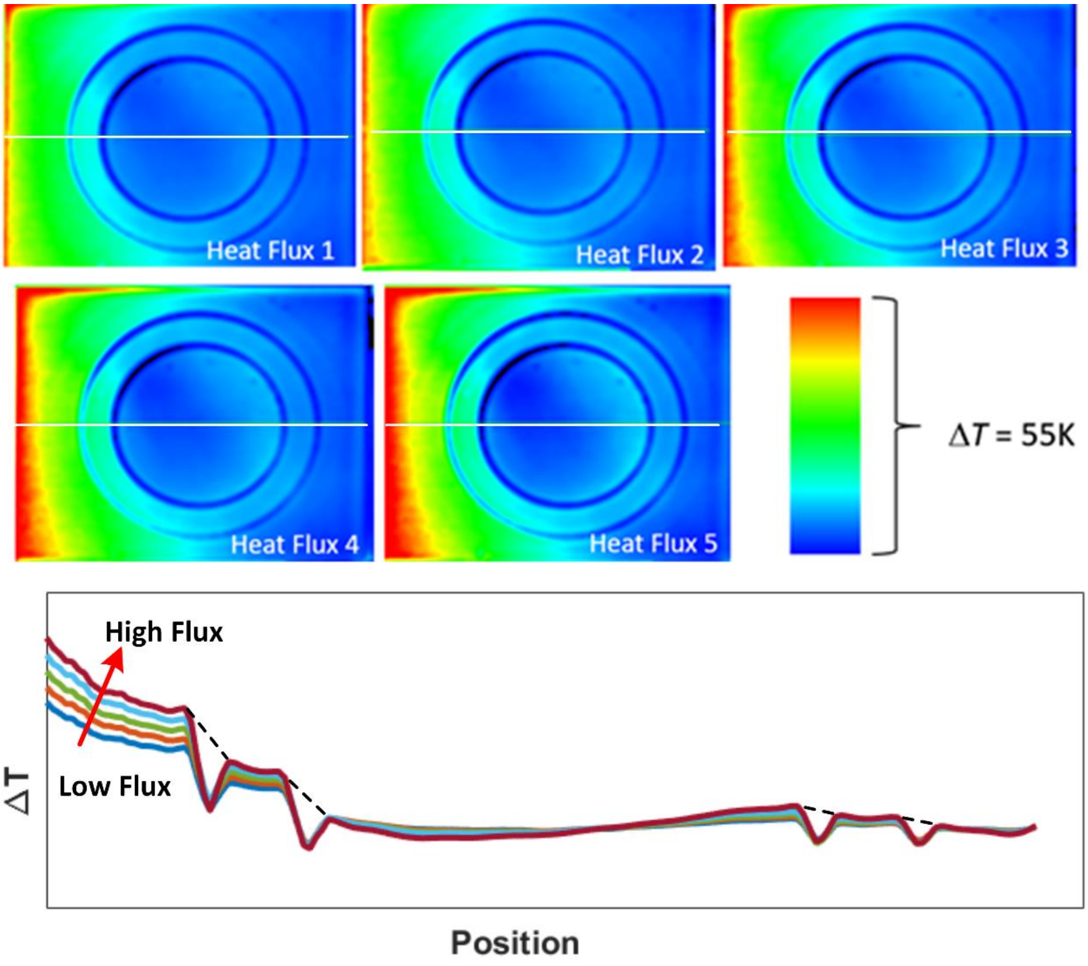

Figure S7: Temperature map of a quadlayer cloak at different heat flux (by increasing temperature bias). It can be seen that although the total heat flux and temperature bias are increased, the temperature linecut in the cloaked region remains flat. This indicates that the heat flux in the region is nearly zero and insensitive to the imposed thermal gradient, which proves the function of thermal cloaking. The dips in the temperature profile on either side of the central region are artifacts due to edge effects at the boundaries at regions of high irradiation intensity, where the TRI signal is not reliable. The black dashed lines have been drawn to show what would be a close estimation of temperature profile in absence of the artifacts on and around high irradiation intensity rings.

Supplementary information references

[1] Dames C.; Chen, G., J. Appl. Phys. 2004, 95, 682.

[2] Yang, F.; Dames, C., Phys. Rev. B, 2013, 87, 035437.

[3] McCurdy, A. K.; Maris, H. J.; Elbaum, C., Phys. Rev. B, 1970, 2, 4077.

[4] Lee, Jaeho; Lee, Woochul; Wehmeyer, Geoff; Dhuey, Scott; Olynick, Deirdre L.; Cabrini, Stefano; Dames, Chris; Urban, Jeffrey J.; Yang, Peidong. Nature Commun. 2017, 8, 14054.

[5] The Stopping and Range of Ions in Matter, http://www.srim.org/

[6] Kendig, D.; Hohensee, G.; Pek, E.; Kuang, W.; Yazawa, K.; Shakouri, A.; in 16th IEEE Intersociety Conference on Thermal and Thermomechanical Phenomena in Electronic Systems (ITherm), 2017, 23.

[7] Christofferson, J.; Maize, K.; Ezzahri, Y.; Shabani, J.; Wang X.; Shakouri, A., Journal of Electronic Packaging, 2008, 130, 041101.

[8] D. Kendig, et al., in 28th Annual IEEE Semiconductor Thermal Measurement and Management Symposium (SEMI-THERM). IEEE, 2012.

[9] Yovanovich, M. M., in *Handbook of Heat Transfer*, edited by Rohsenow, W. M.; Hartnett, J. P.; Cho, Y. L.; McGraw–Hill, New York, 1998, Chap. 3.

[10] Marconnet, A. M.; Asheghi, M.; Goodson, K. E.; J. Heat Transfer, 2013, 135 (6), 061601.

[11] Wehmeyer, G.; Monachon, C.; Yabuki, T.; Wu J.; Dames, C.; Appl. Phys. Rev., 2017, 4, 041304.

[12] Heinrich Hoff, Physica, 1985, 131A, 449.

[13] Dames, C., J. Heat Transfer, 2009, 131, 061301.